Journal of
Materials Chemistry C

Accepted Manuscript

This article can be cited before page numbers have been issued, to do this please use: J. Yan, X. zhang, Y. Pan, J. Li, B. Shi, S. Liu, J. Yang, Z. Song, H. Zhang, M. Ye, R. Quhe, Y. Wang, J. Yang, F. Pan and J. Lu, *J. Mater. Chem. C*, 2018, DOI: 10.1039/C8TC01421C.

ROYAL SOCIETY OF CHEMISTRY

rsc.li/materials-c

View Article Online
DOI: 10.1039/C8TC01421C

Monolayer Tellurene—Metal Contacts

Jiahuan Yan,[1, †] Xiuying Zhang,[1, †] Yuanyuan Pan,[1] Jingzhen Li,[1] Bowen Shi,[1] Shiqi Liu,[1] Jie Yang,[1] Zhigang Song,[1] Han Zhang,[1] Meng Ye,[1] Ruge Quhe,[3] Yangyang Wang,[4] Jinbo Yang,[1,2] Feng Pan,[5,*] and Jing Lu[1, 2,*]

[1]State Key Laboratory for Mesoscopic Physics and Department of Physics, Peking University, Beijing 100871, P. R. China

[2]Collaborative Innovation Center of Quantum Matter, Beijing 100871, P. R. China

[3]State Key Laboratory of Information Photonics and Optical Communications and School of Science, Beijing University of Posts and Telecommunications, Beijing 100876, P. R. China

[4]Nanophotonics and Optoelectronics Research Center, Qian Xuesen Laboratory of Space Technology, China Academy of Space Technology, Beijing 100094, P. R. China

[5]School of Advanced Materials, Peking University, Shenzhen Graduate School, Shenzhen 518055, China

[†]These authors contributed equally to this work.

Email: jinglu@pku.edu.cn, panfeng@pkusz.edu.cn

Abstract

Two-dimensional (2D) atomic crystal is a competitive channel material for next generation electronics for its outstanding gate electrostatics and few dangling bond. Tellurene, a new experimentally accessible Group-VI 2D tellurium, has drawn recent attention for its large on/off ratios, high mobility and significant air stability. We comprehensively examination for the first time the interfacial characteristics of monolayer (ML) tellurene field-effect transistors with a series of common bulk metals and 2D graphene as electrodes by using *ab initio* electronic structure calculation and quantum transport simulation. Furthermore, a lateral *n*-type Schottky contact is formed when contacting with Au in *a* direction and Sc in both directions, while a lateral *p*-type Schottky contact with Au in *b* direction, and Cu, Ni, Ag, Pt, Pd in both directions as a result of a strong Fermi level pinning (FLP). The obtained FLP factor is 0.15 in *a* direction and 0.09 in *b* direction. Remarkably, a highly desirable lateral *p*-type Ohmic contact is formed with graphene in both directions. Our examination gives an insight into the interfacial properties and a guidance in electrode selection for ML tellurene devices.

Keywords: monolayer tellurene, interfacial characteristics, Schottky contact, Ohmic contact, quantum transport simulation, first-principles calculation

View Article Online
DOI: 10.1039/C8TC01421C

Introduction

Two-dimensional (2D) semiconductors have advantage of outstanding gate controllability due to atomic thickness and of few interface traps owning to dangling-bond-free interface, and thus are promising candidate of the channel material for next generation electronic and optoelectronic devices.[1-3] Recently, Group-VI tellurene (2D tellurium Te), a new member of 2D semiconductor family, has been experimentally attained.[4-7] Anisotropic tellurene consists of tetragonal and hexagonal rings (Fig. 1a).[8-9] The band gap of tellurene is from nearly direct 0.33 eV (in bulk) to indirect 0.92 eV (monolayer (ML)).[4, 6, 9-13] Tellurene field effect transistor (FET) experimentally shows a large on/off ratio of 10^6 and a high mobility up to 700 $cm^2/(V \cdot s)$,[6] later of which is higher than that of MoS_2[14-16] and $MoSe_2$.[17-20] Furthermore, tellurene has significant air stability compared with air-sensitive black phosphorene.[6, 21-22] Above all these superiorities allow tellurene to join the competitive 2D channel material rank.

In a practical 2D semiconductor device, the conventional doping method usually is substituted by a direct contact with metal to inject carriers on account of the deficiency of sustainable and controllable substitutional doping methods for 2D materials.[23-24] However, such direct contact induces the formation of Schottky barrier in semiconductor-metal junctions, on account of the Fermi level pinning (FLP) deriving from the interaction between the electrode and channel, which reduces the carrier injection efficiency and then depresses the device performance.[24-25] Therefore, it is important to form low contact resistance by decreasing the Schottky barrier height (SBH) to reveal the prominent intrinsic properties of 2D materials. Obviously, a prediction of the SBH is desirably needed for developing tellurene devices. Experimentally, tellurene transistors have been fabricated with Ni, Pd/Au as electrodes.[6] However, a comprehensive examination of the interfacial properties between ML tellurene and common metals remains absent.

In this article, we carry out a systematical examination for the first time about the interfacial characteristics of ML tellurene with 2D graphene and the metal (Sc, Ag, Cu, Au, Ni, Pt, and Pd) electrodes spanning a wide work function range in a transistor configuration by using *ab initio* electronic structure calculation and quantum transport simulation. The band structures of ML tellurene contacted with bulk metals are heavily hybridized and ML tellurene undergoes a metallization, which mean no SBH existing in the vertical direction. Differently, there is still a

View Article Online
DOI: 10.1039/C8TC01421C

band gap when ML tellurene is placed on top of 2D graphene surface, and a vertical *p*-type Ohmic contact is shaped. A lateral *n*-type Schottky contact is shaped between ML tellurene and Au in *a* direction (with lateral electron SBH of 0.44 eV) and Sc in both *a* and *b* directions (with lateral electron SBH of 0.30 eV and 0.41 eV, respectively). In contrast, a lateral *p*-type Schottky contact is shaped when contacting with Au in *b* direction (with lateral hole SBH of 0.43 eV) and Cu, Ni, Ag, Pt, Pd in both *a* and *b* directions (with lateral hole SBH of 0.45, 0.37, 0.37, 0.28, 0.20 eV in *a* direction and 0.32, 0.42, 0.30, 0.27, 0.28 eV in *b* direction). The formation of the lateral Schottky barrier stems from a strong FLP caused by the metal-induced gap states (MIGS), and the pinning factors are 0.15 and 0.09 in *a* direction and *b* direction, respectively. Remarkably, a highly desirable lateral *p*-type Ohmic contact is formed with graphene in both directions, owing to the match of the work function of ML graphene with the valence band maximum (VBM) of ML tellurene and weak FLP at the interface.

Computational Details

The optimized in-plane lattice constants of ML tetragonal tellurene are a = 4.19 Å and b = 5.49 Å, which are in good accord with the previously computed results.[8-9] We choose the seven metals (Sc, Ag, Cu, Au, Ni, Pt, and Pd) as electrodes, because they cover a wide work function range from 3.58 to 5.65 eV. Besides, experimentally, these metals are commonly used as electrodes in FETs,[26] and tellurene transistors with Ni, Pd/Au as electrodes have been fabricated.[6] We employ six layers of metal atoms to simulate the metal surface because six-layer metal atoms are good enough to characterize a real metal substrate according to the convergence tests carried out in the previous studies.[27-31] The bottom three layers of metal atoms are fixed because ML tellurene interacts mainly with the top layers. Moreover, we adjust the lattice constants of metals and ML graphene to match that of ML tellurene. We adapt 1×2 Au(110)/Ag(110) supercell and $\sqrt{3}$×2 Cu(111)/Ni(111)/ML graphene supercell to a×b ML tellurene supercell and 4×$\sqrt{3}$ Sc(0001)/Pt(111)/Pd(111) supercell to 3a×b ML tellurene supercell. The corresponding mismatches of the lattice constant are within 5%, as shown in Table 1. A vacuum buffer space of more than 15 Å is set to avert pseudo interaction.

When performing the geometry optimizations and electronic structure calculations, we use projector-augmented wave (PAW) pseudopotential[32-33] and a plane-wave basis set with a cut-off energy of 400 eV, implemented in the Vienna *ab initio* simulation package (VASP).[34-37] The

View Article Online
DOI: 10.1039/C8TC01421C

stopping criterion of the geometry optimizations is the residual force below 0.01eV/Å on each atom. For all the calculated structures, the Monkhorst-Pack *k*-point $5\times5\times1$ mesh is sampled for the structural optimizations and $9\times9\times1$ for electronic structure calculations in the Brillouin zone.[38] We take two corrections into account. One is the van der Waals (vdW) interaction with zero damping DFT-D3 method of Grimme.[39] The other is the dipole correction, which is applied to eliminate the pseudo interaction of the dipole moments caused by periodicity in the *z* direction.

A two-probe model is constructed to simulate an FET with a 5-nm channel of ML tellurene and electrodes made of optimized ML tellurene-metal/graphene interfaces, as shown in Fig. 5. The right and left electrodes are semi-infinite. The local device density of states (LDDOS) and the transmission spectra are calculated by using the density functional theory coupled with the non-equilibrium Green's function (NEGF) method implemented in Atomistix ToolKit (ATK) 2016 package.[40-44] The transmission coefficient $T^{k_{||}}(E)$ ($k_{||}$ is a reciprocal lattice vector point along a surface-parallel direction (orthogonal to the transmission direction) in the irreducible Brillouin zone (IBZ)) is calculated as

$$T^{k_{||}}(E) = \mathrm{Tr}[\Gamma_{\mathrm{L}}^{k_{||}}(E)G^{k_{||}}(E)\Gamma_{\mathrm{R}}^{k_{||}}(E)G^{k_{||}\dagger}(E)]$$

where $\Gamma_{\mathrm{L/R}}^{k_{||}}(E) = i(\sum_{\mathrm{L/R}}^{r,k_{||}} - \sum_{\mathrm{L/R}}^{a,k_{||}})$ stands for the level broadening induced by the left electrodes and the right electrodes appearing in the form of the electrode self-energies $\sum_{\mathrm{L/R}}^{k_{||}}$, which is a reflex of the impact of the electrodes on the scattering region[45]. $G^{k_{||}}$ and $G^{k_{||}\dagger}$ is the retarded and advanced Green′s function, respectively. The average of $T^{k_{||}}(E)$ over different $k_{||}$ in the IBZ gives the transmission function at a given energy $T(E)$. A double-ξ polarized (DZP) basis set is employed. The temperature is set at 300 K and the real-space mesh cutoff is of 75 Hartrees. The electronic structures of the electrodes and central region are calculated with a Monkhorst–Pack[38] 50 × 1 ×50 and 50 × 1 × 1 *k*-point grids, respectively. A Dirichlet type, a Neumann type and a periodic type boundary condition[46] are used in the *z*, *y* and *x* directions of the device (see Fig.7), respectively. Additionally, the generalized gradient approximation (GGA) functional to the exchange-correction functional of the Perdew-Burke-Ernzerhof (PBE) form[47] is employed throughout the paper.

Since the 2D semiconductor channel is doped by carriers from the metal electrodes and the

View Article Online
DOI: 10.1039/C8TC01421C

electron-electron interaction is strongly restrained, single electron approximation is effective enough to describe the electron behavior in an FET configuration, so we choose the DFT-GGA in evaluating the SBH.[48-49] For example, the theoretical transport gap of ML, bilayer (BL), and trilayer (TL) black phosphorene with Ni electrode at the DFT-GGA level is 0.65, 0.81 and 0.68 eV,[28, 50-51] respectively, which is in accord with the experimental values (0.99, 0.71 and 0.61 eV for ML, BL and TL,[26] respectively). It's obvious that the DFT-GGA method provides the optimal calculated value. In addition, in the ML/BL/TL phosphorene FET with Ni electrode, the calculated hole (electron) SBH with the DFT-GGA method is 0.26/0.19/0.20 (0.39/0.52/0.48) eV,[28, 50-51] which is in great accord with the observed value of 0.35/0.23/0.21 (0.64/0.48/0.40) eV.[26]

Results and discussion

ML tellurene-metal/graphene interface. After structural optimization, the structure of ML tellurene changes slightly on Sc, Au, Cu, Ni, Ag and graphene surface while strongly on Pt and Pd surface, as shown in Fig. 2. The equilibrium distance d_z is the vertical average distance between ML tellurene and the closest metal layer, shown in Fig. 1(b), and $d_{\text{Te-M}}$ is the minimum atomic distance between the tellurene atom and the metal atom. The binding energy E_b of ML tellurene-metal/graphene system is defined as

$$E_b = (E_{\text{Te}} + E_{\text{M}} - E_{\text{Te-M}}) / N$$

where E_{Te}, E_{M} and $E_{\text{Te-M}}$ are the relaxed energy of the pure ML tellurene, the pure metal/graphene surface and the ML tellurene-metal/graphene systems, respectively, and N is the number of tellurene atom contacted directly with metal. The relevant parameters of ML tellurene-metal/graphene system are listed in Table 1.

According to the binding energy E_b, the interactions between ML tellurene and metal/graphene surface can be divided into three groups. The first is ML tellurene on the ML graphene with weak vdW interaction, characterized by the smallest E_b (0.23 eV) and the largest distance d_z (3.55 Å) and $d_{\text{Te-M}}$ (3.82 Å) among all the contacts. The second is ML tellurene on Au, Ag and Cu surface with moderate adhesion, featured by slightly large E_b (1.76 - 2.23 eV) and small d_z (1.48 - 1.95 Å) and $d_{\text{Te-M}}$ (2.51 - 2.84 Å). The third group is ML on Sc, Ni, Pt and Pd surface with strong adhesion, characterized by quite large E_b (3.00 – 3.36

View Article Online
DOI: 10.1039/C8TC01421C

eV) and small d_z (1.76 - 2.47 Å) and $d_{\text{Te-M}}$ (2.39-2.76 Å).

The differences between the bond strength in the later two groups are ascribed to the different numbers of the unpaired electrons. Free-standing Au ($5d^{10}6s^1$), Ag ($4d^{10}5s^1$) and Cu ($3d^{10}4s^1$) atom have one unpaired electron in the outermost orbital, accompanied by one covalent bond with ML tellurene. Thus, a relative small binding energy is obtained with ML tellurene. Free-standing Ni ($3d^8 4s^2$) and Pt ($5d^9 6s^1$) atoms both have two unpaired electrons and form two covalent bonds with ML tellurene. Free-standing Pd ($4d^{10}$) and Sc ($3d^1 4s^2$) atom have zero and one unpaired electron, respectively. However, according to Mulliken population analysis, Pd and Sc atoms approximately have two and three unpaired electrons ($4d^9 5s^1$ for Pd and $3d^1 4s^1 4p^1$ for Sc), respectively, when they are contacted with tellurene because a hybridization occurs between 4*d* and 5*s* orbitals of Pd atom and between 3*d*, 4*s* and 4*p* orbitals of Sc atom owing to an overlap of *d* orbital with broadened *s* and *p* orbital. Thus, Pd and Sc atoms form two and three covalent bonds with ML tellurene, respectively. Thus, Pd, Sc, Ni and Pt atoms have large binding energy with ML tellurene.

The band structures of free-standing ML tellurene and ML tellurene-metal/graphene systems are shown in Fig. 3. ML tellurene has an indirect band gap of 1.14 eV without spin-orbital coupling, which is in good accord with the previous DFT result of 1.17 eV.[8] The band structures of ML tellurene are strongly destroyed on all the metal surfaces, suggestive of a covalent interaction between ML tellurene and all the checked metals. The hybridization degree of the band structure is much stronger when ML tellurene on Sc, Ni, Pt and Pd surface than on Au, Ag and Cu surface owing to more covalent bonds. Besides, there are some bands of ML tellurene on all the metal surfaces always crossing the Fermi level, suggesting a metallization of ML tellurene. In contrast, the band structure of ML tellurene is preserved well on graphene surface due to weak vdW interaction.

The partial density of states (PDOS) of free-standing ML tellurene and ML tellurene-metal/graphene surfaces are shown in Fig. 4. The band gap disappears for ML tellurene on all the checked metal surfaces, as a result of the hybridization of the band structure and the metallization of ML tellurene. There is a clear band gap of ML tellurene on graphene surface, a fact in great accord with the weak vdW interaction achieved in previous at the interface. The Fermi level is dominated by *p* orbital of ML tellurene.

View Article Online
DOI: 10.1039/C8TC01421C

ML tellurene transistors. A schematic diagram of a ML tellurene transistor is shown in Fig. 5. The Schottky barrier depresses the electron transport and degrades the performance of an FET. There are two kinds of interfaces that possibly present Schottky barrier in a ML tellurene transistor. One is vertical Schottky barrier (Φ_V) at interface A (between the ML tellurene and the metal/graphene surface) in the vertical direction. The other is lateral Schottky barrier (Φ_L) at interface B (between the ML tellurene channel and the electrode) in the lateral *a* (*b*) direction. The lateral SBHs in both methods are shown in Table 1 and Fig. 8.

Φ_V is defined as the difference between the Fermi level and the conduction band minimum (CBM) /VBM at the interface A (Fig. 5) and can be attained from the band structures of ML tellurene-metal/graphene interfaces (Fig. 3) or the LDDOS of ML tellurene transistors at the electrode (Fig. 6 and Fig. 7). The metallization of ML tellurene on seven metal surfaces leads to the absence of the vertical Schottky barrier. On the other hand, the band structure of ML tellurene on graphene surface is preserved well. The Fermi level crosses the valence band of ML tellurene, because the work function of intrinsic ML graphene (4.58 eV) is close to the VBM of intrinsic ML tellurene (4.61 eV). Therefore, the vertical hole SBH (Φ_V^h) is zero, resulting in a vertical *p*-type Ohmic contact on graphene surface.

Φ_L is attained from two methods, the work function approximation (WFA) and more accurate quantum transport simulation. The lateral electron (hole) SBH at the WFA level $\Phi_{L,W}^{e(h)}$ is defined as the difference between the Fermi level of ML tellurene-metal/graphene structure and CBM (VBM) of pure ML tellurene. This method neglects the interaction between the channel ML tellurene and metal/graphene electrode. In the WFA method, a lateral *n*-type Schottky contact is only formed with Sc electrode with the lateral electron SBH ($\Phi_{L,W}^e$) of 0.34 eV. A lateral *p*-type Schottky contact is formed with Au, Cu, Ni, Ag and graphene electrodes with the lateral hole SBH ($\Phi_{L,W}^h$) of 0.10, 0.17, 0.12, 0.37 and 0.06 eV, respectively. Furthermore, a lateral *p*-type Ohmic contact is formed with Pt and Pd.

The lateral electron (hole) SBH at the quantum transport simulation level $\Phi_{L,T}^{e(h)}$ is defined as the difference between the Fermi level and the CBM/VBM at the lateral interface B (Fig. 5) and can be attained from the LDDOS of ML tellurene transistors. The LDDOS and the transmission spectra of the ML tellurene transistors are depicted in Fig. 6 and Fig. 7. The quantum transport

View Article Online
DOI: 10.1039/C8TC01421C

simulation method provides more accurate SBH value than the WFA method, because it takes account of the interaction between the channel ML tellurene and metal/graphene electrode. The interaction leads to FLP, which enhances the difficulty of forming a lateral Ohmic contact.

In the quantum transport simulation, due to the anisotropy of tellurene, we calculate the transport properties of the ML tellurene FETs along both *a* and *b* directions, as shown in Fig. 1(a). In the case of asymmetrical left and right electrodes, we take the average of the lateral SBHs at left and right interfaces. In *a* direction, a lateral *n*-type Schottky contact is formed with Sc and Au with the lateral electron SBH ($\Phi_{\mathrm{L,T}}^{e,a}$) of 0.30 and 0.44 eV, respectively. In contrast, a lateral *p*-type Schottky contact is formed with Pd, Pt, Ni, Ag and Cu with the lateral hole SBH ($\Phi_{\mathrm{L,T}}^{h,a}$) of 0.20, 0.28, 0.37, 0.37 and 0.45 eV in the same direction, respectively. In *b* direction, a lateral *n*-type Schottky contact is only formed with Sc with the lateral electron SBH ($\Phi_{\mathrm{L,T}}^{e,b}$) of 0.41 eV. In contrast, a lateral *p*-type Schottky contact is formed with Pt, Pd, Ag, Cu, Ni and Au with the lateral hole SBH ($\Phi_{\mathrm{L,T}}^{h,b}$) of 0.27, 0.28, 0.30, 0.32, 0.42 and 0.43 eV in *b* direction, respectively. Strikingly, a lateral *p*-type Ohmic contact is formed with graphene electrode in both *a* and *b* direction.

These two directions give nearly the same contact type and similar SBH, except for Au electrode. A weak lateral *n*-type Schottky contact is formed in *a* direction for Au electrode, while a weak lateral *p*-type Schottky contact is formed in *b* direction. The difference is because that the Fermi level of Au electrode is close to the band gap center of ML tellurene. Apparent MIGS are formed at the interface B (Fig. 5) for all the checked metal in both *a* and *b* directions and for graphene electrode in *b* direction, as shown in black dashed irregular polygon in Fig. 6 and Fig. 7. In contrast, there are no MIGS at the interface B for graphene electrode in *a* direction.

The lateral SBHs at the WFA level and the quantum transport simulation level in *a* and *b* direction are compared in Fig. 8. These two methods give roughly the same contact polarity, except for Au electrode. The WFA method gives a lateral *p*-type Schottky contact for Au electrode, while the quantum transport simulation only gives a lateral *p*-type Schottky contact in *b* direction but a lateral *n*-type Schottky contact in *a* direction. The WFA method tends to give smaller lateral hole SBH or even artificial lateral *p*-type Ohmic contact, while the quantum

View Article Online
DOI: 10.1039/C8TC01421C

transport simulation tends to give larger lateral hole SBH. These differences between the two methods suggest FLP at the interface between the metal electrodes and the channel, which is induced by the MIGS at the interface B.

For graphene electrode, the WFA method gives a lateral *p*-type quasi-Ohmic contact with a very small hole SBH of 0.06 eV, because the work function of ML tellurene-graphene system (4.55 eV) is close to the VBM of intrinsic ML tellurene (4.61 eV). The quantum transport simulation gives a lateral *p*-type Ohmic contact for graphene electrode in both *a* and *b* directions. The highly similar contact for graphene electrode given by the two methods is attributed to weak FLP originating from no MIGS in *a* direction and few MIGS in *b* direction (Fig. 7).

Fig. 9(a) shows the lateral electron SBHs from the quantum transport simulation in *a* direction and *b* direction as a function of the metal work functions. The slope S is defined as FLP factor, which describes the degree of FLP. $S = 1$ represents no FLP, and $S = 0$ implies complete pinning. We get a rather low FLP factor of $S_a = 0.15$ and $S_b = 0.09$ in *a* direction and *b* direction, respectively, indicating a strong FLP at the interface B and the stronger FLP in *b* direction than in *a* direction. This FLP is illustrated more explicitly in Fig. 9(b), where the Fermi level is pinned from the 0.3 eV below the CBM to the VBM of the ML tellurene. Both of the FLP factors of ML tellurene are smaller than theoretical $S = 0.27$ of ML MoS_2,[52] $S = 0.28$ of ML black phosphorene,[28] $S = 0.33$ of ML arsenene,[53-54] and $S = 0.42$ of ML blue phosphorene,[55] implying a stronger FLP at interface B of ML tellurene.

Since the metals and ML graphene are stretched to match tellurene in our model, the SBHs will be affected in light of the work function change with the strain of the metals and ML graphene. To explore the effect of the lattice mismatch of the metals and ML graphene on the SBH, we choose the metal Ni, which has the maximal mismatch in all the checked metals, and ML graphene. On account of the strain, the work function varies from 5.08 to 5.01 eV for metal Ni and from 4.61 to 4.58 eV for ML graphene. These small changes indicate that the SBH only changes by 0.07 eV for metal Ni and 0.04 eV for ML graphene at WFA level. On the other hand, the change of the SBH at the quantum transport simulation level is expected to be smaller than 0.07 eV for metal Ni electrode and 0.04 eV for ML graphene electrode because of the existence of Fermi level pinning at the interface between the channel and the electrodes. Thus, the

View Article Online
DOI: 10.1039/C8TC01421C

mismatch in our study has very slight effect on the SBHs in both methods.

The transport gap E_g^a (E_g^b) is defined as the sum of the lateral electron and hole SBH of $\Phi_{L,T}^{e,a}$ ($\Phi_{L,T}^{e,b}$) and $\Phi_{L,T}^{h,a}$ ($\Phi_{L,T}^{h,b}$) in *a* (*b*) direction, that is, $E_g^a = \Phi_{L,T}^{e,a} + \Phi_{L,T}^{h,a}$ ($E_g^b = \Phi_{L,T}^{e,b} + \Phi_{L,T}^{h,b}$). E_g^a (E_g^b) of ML tellurene transistor with Sc, Au, Cu, Ni, Ag, Pt, Pd and graphene is 0.97, 0.98, 1.03, 0.99, 0.96, 0.97, 1.00 and 1.00 eV (0.98, 0.96, 1.02, 1.00, 1.00, 1.01, 0.97 and 0.97 eV), respectively, listed in Table. 1. E_g^a and E_g^b are close to each other and comparable with the band gap of free- standing ML tellurene (1.14 eV).

Discussion

It was shown that ML black phosphorene prefers a lateral *p*-type Schottky contact with metals both experimentally and theoretically.[19, 27] Our examination suggests that ML tellurene also prefers a lateral *p*-type Schottky contact with metal electrodes, due to its small work function of 4.61 eV, which is comparable with the calculated one (4.57 eV) of ML black phosphorene.[28] In experiment, tellurene with thickness more than 5 nm forms a lateral *p*-type Ohmic contact with Pd electrode, [6] while in our examination ML tellurene forms a lateral *p*-type Schottky contact. Such a difference is attributed to the fact that the band gap of tellurene decreases and the VBM of tellurene rises with the increase of the layer number, and thus a *p*-type Ohmic contact is favored in multilayer tellurene.

ML black phosphorene cannot form Ohmic contact with the common metal electrodes in terms of the quantum transport simulation, but a *p*-type Ohmic contact is formed with graphene electrode. [28, 56] Fortunately, in our examination, ML tellurene also forms a lateral *p*-type Ohmic contact with graphene electrode in both directions despite of the Schottky contact with metal electrode. Hence graphene is the optimal electrode material for ML tellurene transistor and high performance is expected.

Conclusion

In summary, we provide comprehensive of the interfacial properties of ML tellurene with bulk metal and 2D graphene electrodes by using *ab initio* electronic structure calculation and quantum transport simulation. A lateral *n*-type Schottky contact is formed with Sc electrode in both directions and Au electrode in *a* direction. A lateral *p*-type Schottky contact is formed

View Article Online
DOI: 10.1039/C8TC01421C

with Cu, Ni, Ag, Pd and Pt electrode in both directions and Au electrode in *b* direction. The lateral Schottky barrier is caused by strong FLP with the FLP factor S_a = 0.15 and S_b = 0.09 and the strong FLP is induced by MIGS at the interface B. Remarkably, ML tellurene forms a lateral *p*-type Ohmic contact with graphene electrode in both directions, owing to the match of the work function of ML graphene with the VBM of ML tellurene and weak FLP at the interface. Therefore, graphene is the optimal electrode material for ML tellurene transistor. Our systemic examination provides a decent reference for the choice of an appropriate electrode in the ML tellurene devices.

View Article Online
DOI: 10.1039/C8TC01421C

Acknowledgement

This work was supported by the National Natural Science Foundation of China (No. 11274016/11474012/11674005/11274233/11664026), the National Basic Research Program of China (No. 2013CB932604/2012CB619304), the Ministry of Science and Technology (National Materials Genome Project) of China (No. 2016YFB0700600/2016YFA0301300). We would like to thank Prof. Peide D. Ye and Dr. Gang Qiu for helpful discussions.

View Article Online
DOI: 10.1039/C8TC01421C

References

(1) Fiori, G.; Bonaccorso, F.; Iannaccone, G.; Palacios, T.; Neumaier, D.; Seabaugh, A.; Banerjee, S. K.; Colombo, L. Electronics Based on Two-dimensional Materials. *Nat. Nanotechnol.* **2014,** *9* (10), 768-779.

(2) Kang, J.; Liu, W.; Sarkar, D.; Jena, D.; Banerjee, K. Computational Study of Metal Contacts to Monolayer Transition-Metal Dichalcogenide Semiconductors. *Phys. Rev. X* **2014,** *4* (3), 031005.

(3) Schwierz, F.; Pezoldt, J.; Granzner, R. Two-dimensional Materials and Their Prospects inTransistor Electronics. *Nanoscale* **2015,** *7* (18), 8261-8283.

(4) Huang, X.; Guan, J.; Lin, Z.; Liu, B.; Xing, S.; Wang, W.; Guo, J. Epitaxial Growth and Band Structure of Te Film on Graphene. *Nano Lett.* **2017,** *17* (8), 4619-4623.

(5) Du, Y.; Qiu, G.; Wang, Y.; Si, M.; Xu, X.; Wu, W.; Ye, P. D. One-Dimensional van der Waals Material Tellurium: Raman Spectroscopy under Strain and Magneto-Transport. *Nano Lett.* **2017,** *17* (6), 3965-3973.

(6) Wang, Y.; Qiu, G.; Wang, Q.; Liu, Y.; Du, Y.; Wang, R.; III, W. A. G.; Kim, M. J.; Ye, P. D.; Wu, W. Large-area Solution-grown 2D Tellurene for Air-stable, High-performance Field-effect Transistors. *arXiv:1704.06202* **2017**.

(7) Churchill, H. O. H.; Salamo, G. J.; Yu, S. Q.; Hironaka, T.; Hu, X.; Stacy, J.; Shih, I. Toward Single Atom Chains with Exfoliated Tellurium. *Nanoscale Res. Lett.* **2017,** *12*, 6.

(8) Zhu, Z.; Cai, X.; Yi, S.; Chen, J.; Dai, Y.; Niu, C.; Guo, Z.; Xie, M.; Liu, F.; Cho, J. H.; Jia, Y.; Zhang, Z. Multivalency-Driven Formation of Te-Based Monolayer Materials: A Combined First-Principles and Experimental study. *Phys. Rev. Lett.* **2017,** *119* (10), 106101.

(9) Zhu, Z.; Cai, C.; Niu, C.; Wang, C.; Sun, Q.; Jia, Y. Tellurene-a Monolayer of Tellurium from First-principles Prediction. *arXiv:1605.03253* **2016**.

(10) Coker, A.; Lee, T.; Das, T. P. Investigation of the Electronic-properties of Tellurium-energy-band Structure. *Phys. Rev. B* **1980,** *22* (6), 2968-2975.

(11) Vonhippel, A. Structure and Conductivity in the VIB Group of the Periodic System. *J. Chem. Phys.* **1948,** *16* (4), 372-380.

(12) Anzin, V. B.; Eremets, M. I.; Kosichkin, Y. V.; Nadezhdinskii, A. I.; Shirokov, A. M. Measurement of Energy-gap in Tellurium under Pressure. *Phys. Status Solidi (a)* **1977,** *42* (1), 385-390.

(13) Cherin, P.; Unger, P. 2-dimensional Refinement of Crystal Structure of Tellurium. *Acta Crystallogr.* **1967,** *23*, 670.

(14) Kim, S.; Konar, A.; Hwang, W. S.; Lee, J. H.; Lee, J.; Yang, J.; Jung, C.; Kim, H.; Yoo, J. B.; Choi, J. Y.; Jin, Y. W.; Lee, S. Y.; Jena, D.; Choi, W.; Kim, K. High-Mobility and Low-power Thin-film Transistors Based on Multilayer MoS2 Crystals. *Nat. Commun.* **2012,** *3*, 7.

(15) Bao, W. Z.; Cai, X. H.; Kim, D.; Sridhara, K.; Fuhrer, M. S. High Mobility Ambipolar MoS_2 Field-effect Transistors: Substrate and Dielectric Effects. *Appl. Phys. Lett.* **2013,** *102* (4), 4.

(16) Jariwala, D.; Sangwan, V. K.; Late, D. J.; Johns, J. E.; Dravid, V. P.; Marks, T. J.; Lauhon, L. J.; Hersam, M. C. Band-like Transport in High Mobility Unencapsulated Single-layer MoS_2 Transistors. *Appl. Phys. Lett.* **2013,** *102* (17), 4.

(17) Larentis, S.; Fallahazad, B.; Tutuc, E. Field-effect Transistors and Intrinsic Mobility in Ultra-thin $MoSe_2$ Layers. *Appl. Phys. Lett.* **2012,** *101* (22), 4.

(18) Chamlagain, B.; Li, Q.; Ghimire, N. J.; Chuang, H. J.; Perera, M. M.; Tu, H. G.; Xu, Y.; Pan, M.; Xaio, D.; Yan, J. Q.; Mandrus, D.; Zhou, Z. X. Mobility Improvement and Temperature Dependence in MoSe2 Field-Effect Transistors on Parylene-C Substrate. *ACS Nano* **2014,** *8* (5), 5079-5088.

View Article Online
DOI: 10.1039/C8TC01421C

(19) Pradhan, N. R.; Rhodes, D.; Xin, Y.; Memaran, S.; Bhaskaran, L.; Siddiq, M.; Hill, S.; Ajayan, P. M.; Balicas, L. Ambipolar Molybdenum Diselenide Field-Effect Transistors: Field-Effect and Hall Mobilities. *ACS Nano* **2014,** *8* (8), 7923-7929.

(20) Wang, X. L.; Gong, Y. J.; Shi, G.; Chow, W. L.; Keyshar, K.; Ye, G. L.; Vajtai, R.; Lou, J.; Liu, Z.; Ringe, E.; Tay, B. K.; Ajayan, P. M. Chemical Vapor Deposition Growth of Crystalline Mono layer $MoSe_2$. *ACS Nano* **2014,** *8* (5), 5125-5131.

(21) Li, L. K.; Yu, Y. J.; Ye, G. J.; Ge, Q. Q.; Ou, X. D.; Wu, H.; Feng, D. L.; Chen, X. H.; Zhang, Y. B. Black Phosphorus Field-effect Transistors. *Nat. Nanotechnol.* **2014,** *9* (5), 372-377.

(22) Liu, H.; Neal, A. T.; Zhu, Z.; Luo, Z.; Xu, X.; Tomanek, D.; Ye, P. D. Phosphorene: An Unexplored 2D Semiconductor with a High Hole Mobility. *ACS Nano* **2014,** *8* (4), 4033-4041.

(23) Liu, H.; Du, Y. C.; Deng, Y. X.; Ye, P. D. Semiconducting Black Phosphorus: Synthesis, Transport Properties and Electronic Applications. *Chem. Soc. Rev.* **2015,** *44* (9), 2732-2743.

(24) Allain, A.; Kang, J. H.; Banerjee, K.; Kis, A. Electrical Contacts to Two-dimensional Semiconductors. *Nat. Mater.* **2015,** *14* (12), 1195-1205.

(25) Das, S.; Demarteau, M.; Roelofs, A. Ambipolar Phosphorene Field Effect Transistor. *ACS Nano* **2014,** *8* (11), 11730-11738.

(26) Das, S.; Zhang, W.; Demarteau, M.; Hoffmann, A.; Dubey, M.; Roelofs, A. Tunable Transport Gap in Phosphorene. *Nano Lett.* **2014,** *14* (10), 5733-5739.

(27) Wang, Y.; Li, J.; Xiong, J.; Pan, Y.; Ye, M.; Guo, Y.; Zhang, H.; Quhe, R.; Lu, J. Does the Dirac Cone of Germanene Exist on Metal Substrates? *Phys. Chem. Chem. Phys.* **2016,** *18* (28), 19451-19456.

(28) Pan, Y.; Wang, Y.; Ye, M.; Quhe, R.; Zhong, H.; Song, Z.; Peng, X.; Yu, D.; Yang, J.; Shi, J.; Lu, J. Monolayer Phosphorene-Metal Contacts. *Chem. Mater.* **2016,** *28* (7), 2100-2109.

(29) Pan, Y.; Li, S.; Ye, M.; Quhe, R.; Song, Z.; Wang, Y.; Zheng, J.; Pan, F.; Guo, W.; Yang, J.; Lu, J. Interfacial Properties of Monolayer $MoSe_2$-Metal Contacts. *J. Phys. Chem. C* **2016,** *120* (24), 13063-13070.

(30) Kang, J. H.; Liu, W.; Sarkar, D.; Jena, D.; Banerjee, K. Computational Study of Metal Contacts to Monolayer Transition-Metal Dichalcogenide Semiconductors. *Phys. Rev. X* **2014,** *4* (3), 031005.

(31) Zheng, J.; Wang, Y.; Wang, L.; Quhe, R.; Ni, Z.; Mei, W.-N.; Gao, Z.; Yu, D.; Shi, J.; Lu, J. Interfacial Properties of Bilayer and Trilayer Graphene on Metal Substrates. *Sci. Rep.* **2013,** *3*, 2081.

(32) Kresse, G.; Joubert, D. From Ultrasoft Pseudopotentials to the Projector Augmented-wave Method. *Phys. Rev. B: Condens. Matter Mater. Phys.* **1999,** *59*, 1758-1775.

(33) Blöchl, P. E. Projector Augmented-wave Method. *Phys. Rev. B* **1994,** *50* (24), 17953-17979.

(34) Kresse, G.; Hafner, J. Abinitio Molecular-Dynamics For Liquid-Metals. *Phys. Rev. B* **1993,** *47* (1), 558-561.

(35) Kresse, G.; Hafner, J. Ab-initio Molecular-Dynamic Simulation of the Liquid-Metal Amorphous-Semiconductor Transition in Germanium. *Phys. Rev. B* **1994,** *49* (20), 14251-14269.

(36) Kresse, G.; Furthmuller, J. Efficiency of Ab-initio Total Energy Calculations for Metals and Semiconductors Using a Plane-wave Basis Set. *Comput. Mater. Sci.* **1996,** *6* (1), 15-50.

(37) Kresse, G.; Furthmuller, J. Efficient Iterative Schemes for Ab initio Total-energy Calculations Using a Plane-wave Basis Set. *Phys. Rev. B* **1996,** *54* (16), 11169-11186.

(38) Monkhorst, H. J.; Pack, J. D. Special Points For Brillouin-Zone Integrations. *Phys. Rev. B* **1976,** *13* (12), 5188-5192.

(39) Grimme, S.; Antony, J.; Ehrlich, S.; Krieg, H. A consistent and accurate ab initio parametrization of density functional dispersion correction (DFT-D) for the 94 elements H-Pu. *J. Chem. Phys.* **2010,** *132*

View Article Online
DOI: 10.1039/C8TC01421C

(15), 19.

(40) Yuan, Y.; Quhe, R.; Zheng, J.; Wang, Y.; Ni, Z.; Shi, J.; Lu, J. Strong Band Hybridization between Silicene and Ag(111) Substrate. *Physica E* **2014,** *58*, 38-42.

(41) Brandbyge, M.; Mozos, J. L.; Ordejon, P.; Taylor, J.; Stokbro, K. Density-functional Method for Nonequilibrium Electron Transport. *Phys. Rev. B* **2002,** *65* (16), 165401.

(42) *Atomistix ToolKit*, version 2016; QuantumWise A/S: Copenhagen, Denmark, 2017. http://www.quantumwise.com (accessed Jun 9, 2017).

(43) Soler, J. M.; Artacho, E.; Gale, J. D.; Garcia, A.; Junquera, J.; Ordejon, P.; Sanchez-Portal, D. The SIESTA Method for Ab Initio Order-N Materials Simulation. *J. Phys.-Condes. Matter* **2002,** *14* (11), 2745-2779.

(44) Smith, D. R.; Schultz, S.; Markos, P.; Soukoulis, C. M. Determination of Effective Permittivity and Permeability of Metamaterials from Reflection and Transmission Coefficients. *Phys. Rev. B* **2002,** *65* (19), 5.

(45) Cakir, D.; Peeters, F. M. Dependence of the Electronic and Transport Properties of Metal-$MoSe_2$ Interfaces on Contact Structures. *Phys. Rev. B* **2014,** *89* (24), 7.

(46) Cheng, A. H. D.; Cheng, D. T. Heritage and Early History of the Boundary Element Method. *Eng. Anal. Bound. Elem.* **2005,** *29* (3), 268-302.

(47) Perdew, J. P.; Burke, K.; Ernzerhof, M. Generalized Gradient Approximation Made Simple. *Phys. Rev. Lett.* **1996,** *77* (18), 3865-3868.

(48) Quhe, R.; Fei, R.; Liu, Q.; Zheng, J.; Li, H.; Xu, C.; Ni, Z.; Wang, Y.; Yu, D.; Gao, Z.; Lu, J. Tunable and Sizable Band Gap in Silicene by Surface Adsorption. *Sci. Rep.* **2012,** *2*, 853.

(49) Liang, Y.; Yang, L. Carrier Plasmon Induced Nonlinear Band Gap Renormalization in Two-dimensional Semiconductors. *Phys. Rev. Lett.* **2015,** *114* (6), 063001.

(50) Pan, Y.; Dan, Y.; Wang, Y.; Ye, M.; Zhang, H.; Quhe, R.; Zhang, X.; Li, J.; Guo, W.; Yang, L.; Lu, J. Schottky Barriers in Bilayer Phosphorene Transistors. *ACS Appl. Mater. Interfaces* **2017,** *9* (14), 12694-12705.

(51) Zhang, X.; Pan, Y.; Ye, M.; Quhe, R.; Wang, Y.; Guo, Y.; Zhang, H.; Dan, Y.; Song, Z.; Li, J.; Yang, J.; Guo, W.; Lu, J. Three-layer Phosphorene-metal Interfaces. *Nano Res.* **2017**, DOI: 10.1007/s12274-017-1680-6.

(52) Zhong, H.; Quhe, R.; Wang, Y.; Ni, Z.; Ye, M.; Song, Z.; Pan, Y.; Yang, J.; Yang, L.; Lei, M.; Shi, J.; Lu, J. Interfacial Properties of Monolayer and Bilayer MoS_2 Contacts with Metals: Beyond the Energy Band Calculations. *Sci. Rep.* **2016,** *6*, 21786.

(53) Wang, Y.; Ye, M.; Weng, M.; Li, J.; Zhang, X.; Zhang, H.; Guo, Y.; Pan, Y.; Xiao, L.; Liu, J.; Pan, F.; Lu, J. Electrical Contacts in Monolayer Arsenene Devices. *ACS Appl. Mater. Interfaces* **2017,** *9* (34), 29273-29284.

(54) Guo, Y.; Liu, D.; Robertson, J. 3D Behavior of Schottky Barriers of 2D Transition-Metal Dichalcogenides. *ACS Appl. Mater. Interfaces* **2015,** *7* (46), 25709-25715.

(55) Li, J.; Sun, X.; Xu, C.; Zhang, X.; Pan, Y.; Ye, M.; Song, Z.; Quhe, R.; Wang, Y.; Zhang, H.; Guo, Y.; Yang, J.; Pan, F.; Lu, J. Electrical Contacts in Monolayer Blue Phosphorene. *Nano Res.* **2017**, DOI: 10.1007/s12274-017-1801-2.

(56) Quhe, R.; Peng, X.; Pan, Y.; Ye, M.; Wang, Y.; Zhang, H.; Feng, S.; Zhang, Q.; Shi, J.; Yang, J.; Yu, D.; Lei, M.; Lu, J. Can a Black Phosphorus Schottky Barrier Transistor Be Good Enough? *ACS Appl. Mater. Interfaces* **2017,** *9* (4), 3959-3966.

View Article Online
DOI: 10.1039/C8TC01421C

Table 1. Calculated Interlayer Properties of ML tellurene-Metal Contacts. $\bar{\varepsilon}$ is the average lattice constant mismatch between the metal surface and ML tellurene. The equilibrium distance d_z is the average distance between the contact ML tellurene-metal interfaces in the vertical direction. $d_{\text{Te-M}}$ is the minimum atom-to-atom distance from the tellurene atom to the metal atom. The binding energy E_b is the energy per tellurium atom to remove ML tellurene from the metal surface. W_M and $W_{\text{Te-M}}$ are the calculated WF for clean metal surface and the ML tellurene-metal system, respectively. $\Phi^e_{L,W}$ ($\Phi^h_{L,W}$) is the electron (hole) SBH obtained from the WFA in the lateral. $\Phi^{e,a}_{L,T}$ and $\Phi^{e,b}_{L,T}$ ($\Phi^{h,a}_{L,T}$ and $\Phi^{h,b}_{L,T}$) are the electron (hole) transport SBHs obtained from the quantum transport simulation in the lateral *a* direction and *b* direction, respectively. E^a_g and E^b_g are the transmission gaps in *a* direction and *b* direction, respectively.

Metal	Sc	Au	Cu	Ni	Ag	Pt	Pd	graphene
$\bar{\varepsilon}$ (%)	3.23	2.35	4.40	4.51	2.35	3.27	3.60	4.57
d_z (Å)	2.47	1.78	1.95	1.76	1.48	2.20	2.15	3.55
$d_{\text{Te-M}}$ (Å)	2.76	2.84	2.51	2.39	2.82	2.57	2.53	3.82
E_b (eV)	3.00	1.76	2.23	3.04	1.86	3.33	3.36	0.23
W_M (eV)	3.58	4.96	4.60	5.01	4.19	5.65	5.12	4.58
$W_{\text{Te-M}}$ (eV)	3.81	4.52	4.45	4.50	4.24	4.87	4.62	4.55
$\Phi^e_{L,W}$ (eV)	0.34	1.05	0.98	1.02	0.77	1.40	1.15	1.08
$\Phi^h_{L,W}$ (eV)	0.80	0.10	0.17	0.12	0.37	-0.26	-0.01	0.06
$\Phi^{e,a}_{L,T}$ (eV)	0.30	0.44	0.58	0.62	0.59	0.69	0.80	1.00
$\Phi^{h,a}_{L,T}$ (eV)	0.67	0.54	0.45	0.37	0.37	0.28	0.20	0
$\Phi^{e,b}_{L,T}$ (eV)	0.41	0.53	0.70	0.58	0.70	0.74	0.69	0.97
$\Phi^{h,b}_{L,T}$ (eV)	0.57	0.43	0.32	0.42	0.30	0.27	0.28	0
E^a_g (eV)	0.97	0.98	1.03	0.99	0.96	0.97	1.00	1.00
E^b_g (eV)	0.98	0.96	1.02	1.00	1.00	1.01	0.97	0.97

View Article Online
DOI: 10.1039/C8TC01421C

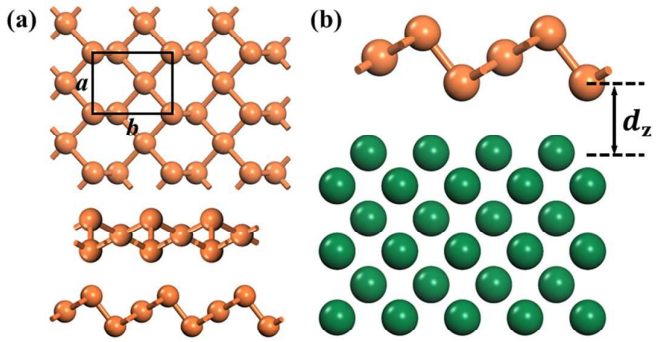

Figure 1. (a) Top and side views of free-standing ML tellurene. (b) Initial configuration of ML tellurene on the metal surface (green ball).

View Article Online
DOI: 10.1039/C8TC01421C

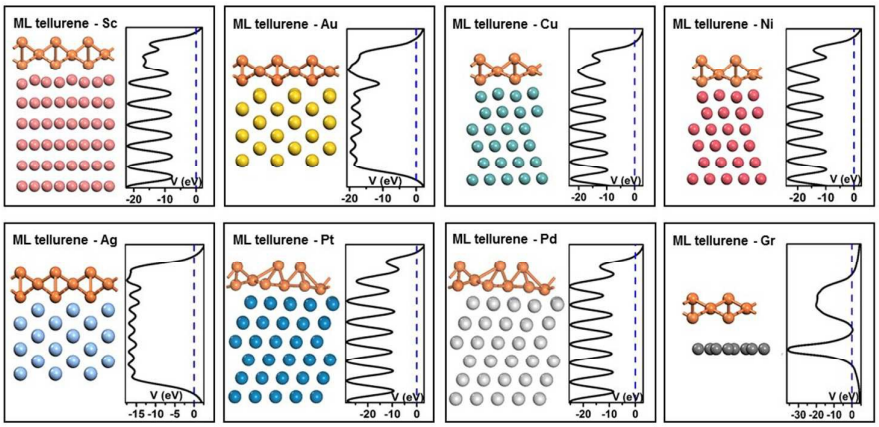

Figure 2. Side view of the optimized structure and average electrostatic potential distribution in planes normal to the interface of ML tellurene on Sc, Au, Cu, Ni, Ag, Pt, Pd and graphene surfaces, respectively. The Fermi level is set to zero and denoted by blue dashed line.

View Article Online
DOI: 10.1039/C8TC01421C

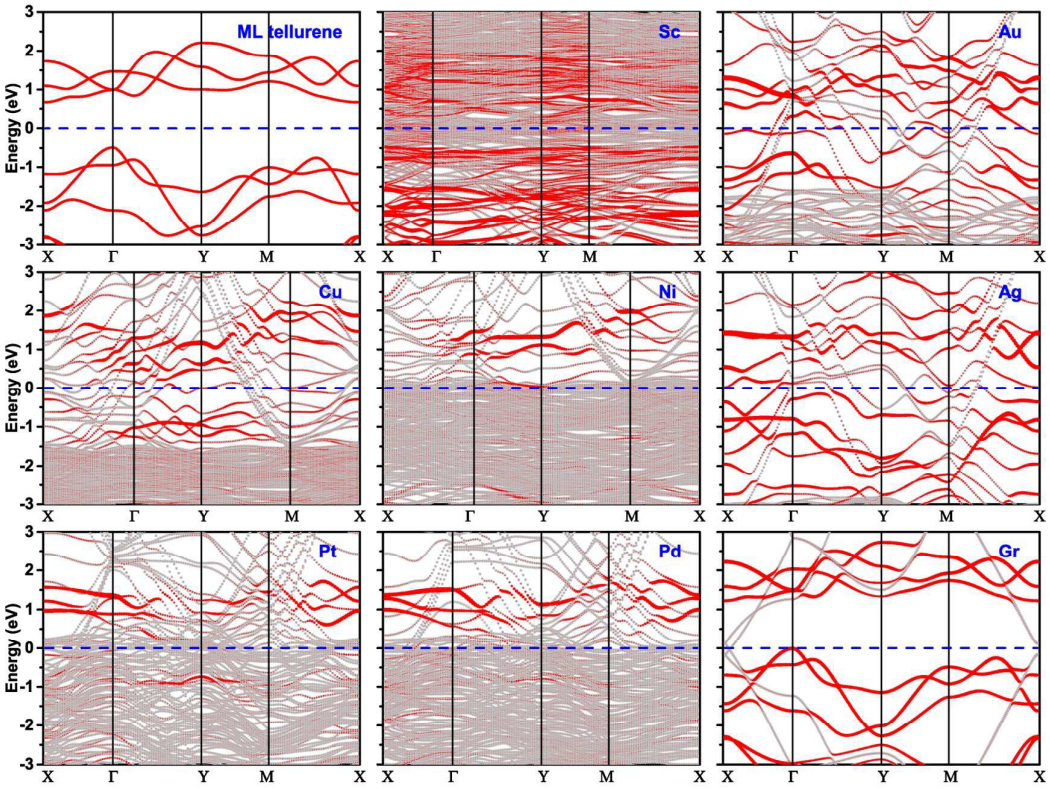

Figure 3. Band structures of ML tellurene and the ML tellurene-metal systems (projected to the ML tellurene). Gray line: band structure of the interfacial systems; Red line: band structures projected to the ML tellurene. The Fermi level is set at zero energy and denoted by blue dashed line.

View Article Online
DOI: 10.1039/C8TC01421C

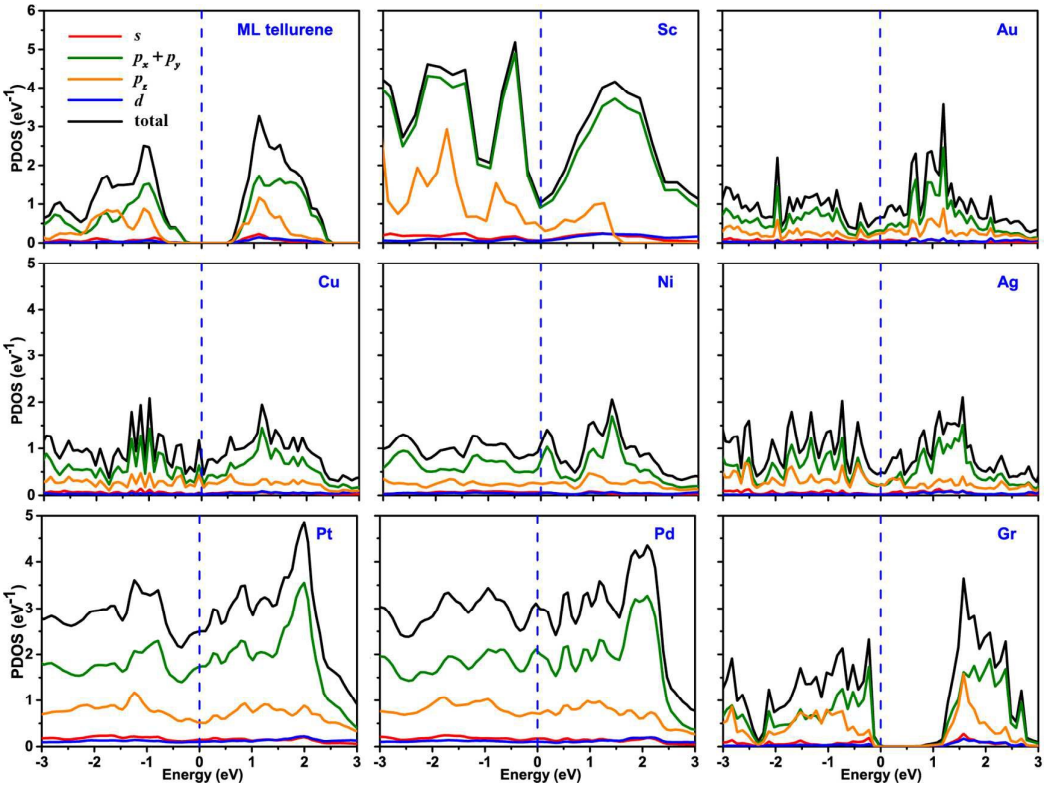

Figure 4. Partial density of states (PDOS) of ML tellurene and ML tellurene on the metal surfaces from the energy band calculations. The Fermi level is set at zero energy and denoted by vertical blue dashed lines.

View Article Online
DOI: 10.1039/C8TC01421C

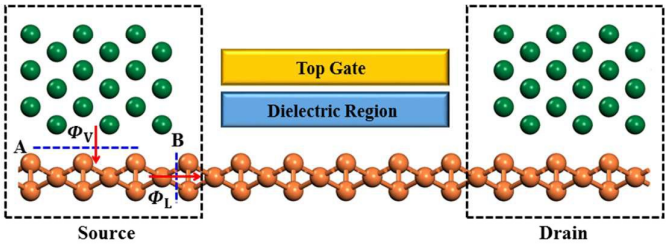

Figure 5. Schematic diagrams of ML tellurene FETs. Blue dashed lines donate the interfaces where Schottky barriers may exist. Φ_V and Φ_L represent the vertical SBH and the lateral SBH, respectively. Red rows represent the pathways that the electrons or holes transfer through the interfaces shown in blue dashed lines.

View Article Online
DOI: 10.1039/C8TC01421C

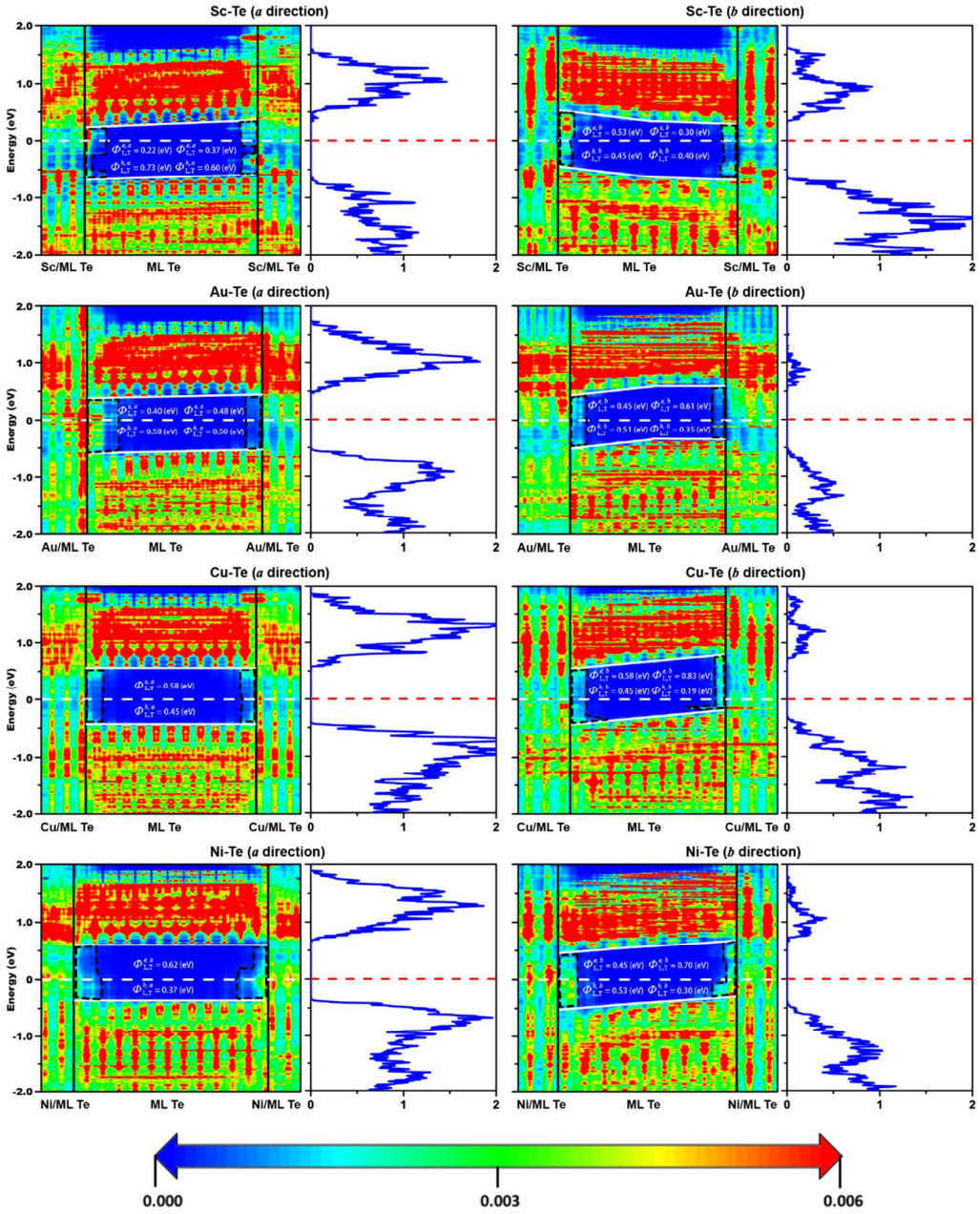

Figure 6. Zero-bias and zero-gate voltage LDDOS (left panel) and transmission spectra (right panel) of the ML tellurene FETs with Sc, Au, Cu and Ni electrode, respectively, and a channel length of L = 5 nm. $\Phi^{e,a}_{\mathrm{L,T}}$ ($\Phi^{e,b}_{\mathrm{L,T}}$) and $\Phi^{h,a}_{\mathrm{L,T}}$ ($\Phi^{h,b}_{\mathrm{L,T}}$) represent the electron SBH and hole SBH in the lateral a (b) direction, respectively. The Fermi level is represented by a white and red dashed line, respectively. MIGS are encircled by a black dashed line. The color scale is shown below the plot.

View Article Online
DOI: 10.1039/C8TC01421C

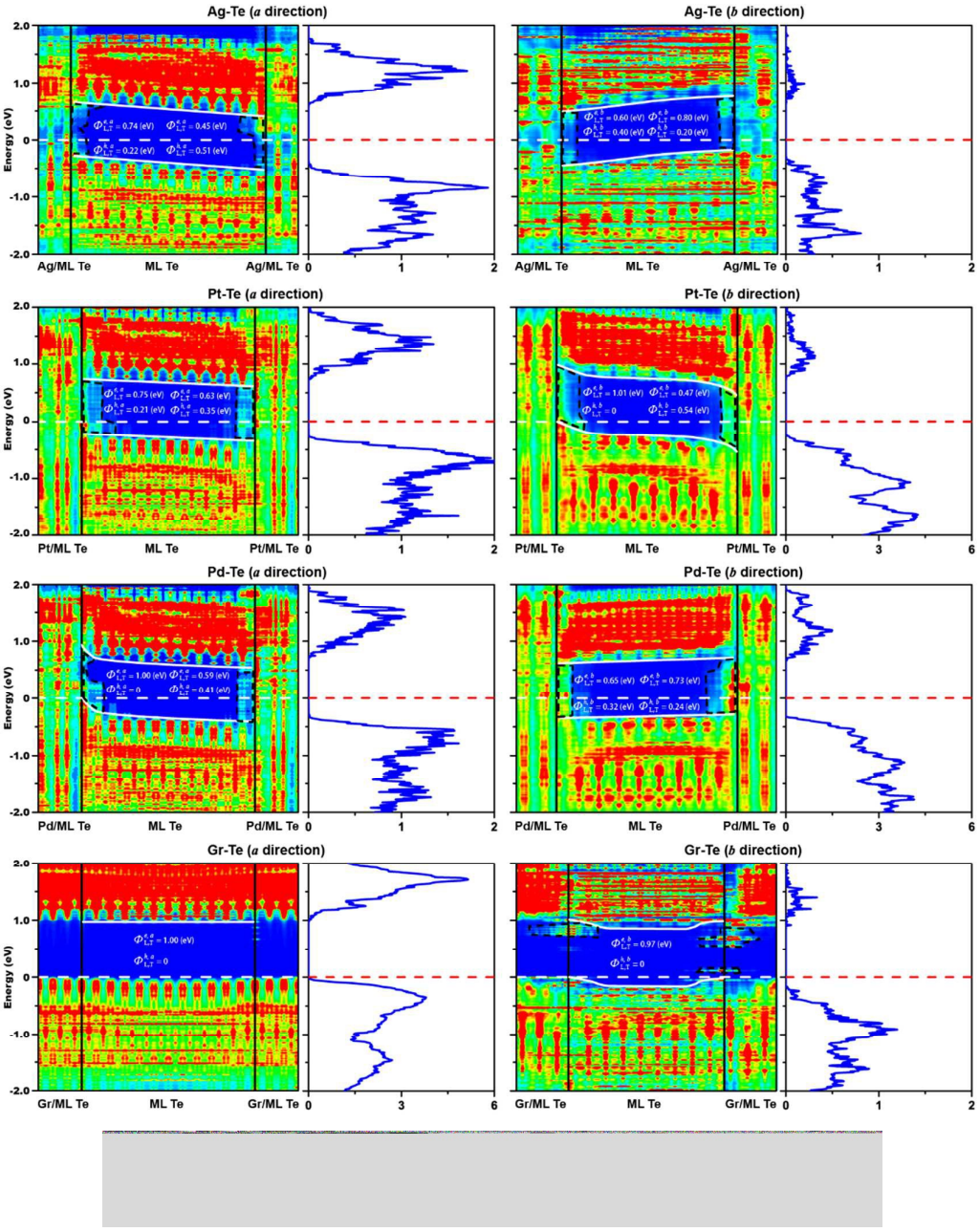

Figure 7. Zero-bias and zero-gate voltage LDDOS (left panel) and transmission spectra (right panel) of the ML tellurene FETs with Ag, Pt, Pd and graphene electrode, respectively, and a channel length of L = 5 nm. $\Phi^{e,a}_{\mathrm{L,T}}$ ($\Phi^{e,b}_{\mathrm{L,T}}$) and $\Phi^{h,a}_{\mathrm{L,T}}$ ($\Phi^{h,b}_{\mathrm{L,T}}$) represent the electron SBH and hole SBH in the lateral a (b) direction, respectively. The Fermi level is represented by a white and red dashed line, respectively. MIGS are encircled by a black dashed line. The color scale is shown below the plot.

View Article Online
DOI: 10.1039/C8TC01421C

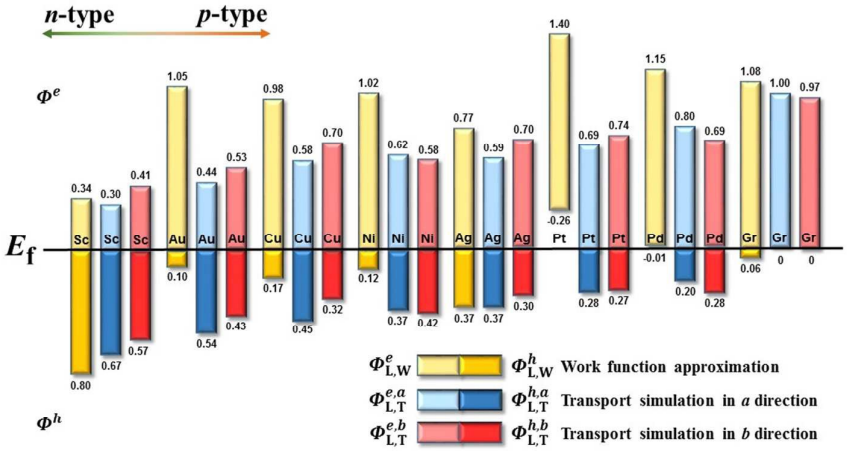

Figure 8. Comparison of the lateral SBHs in ML tellurene FET obtained from the work function approximation ($\Phi^{e/h}_{L,W}$) and the quantum transport simulation in the *a* ($\Phi^{e/h,a}_{L,T}$) direction and *b* ($\Phi^{e/h,b}_{L,T}$) direction.

View Article Online
DOI: 10.1039/C8TC01421C

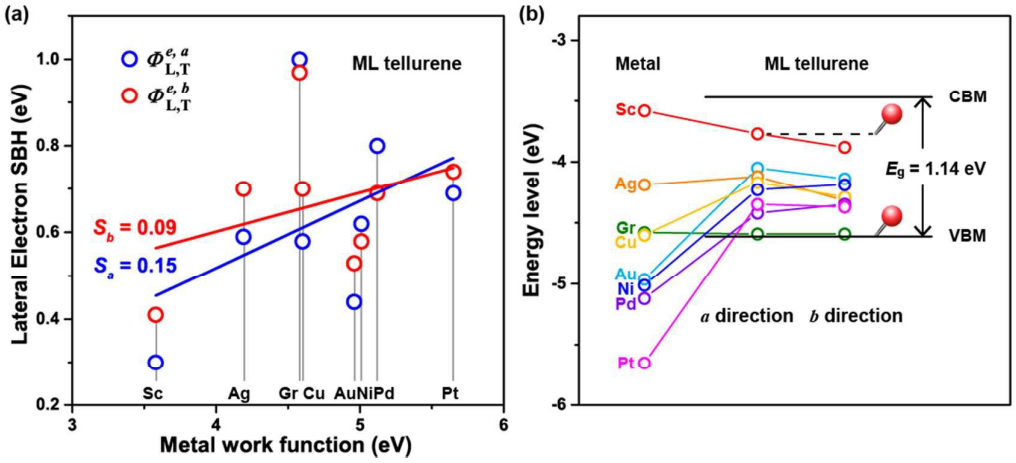

Figure 9. (a) Comparison of the lateral electron SBH as a function of the metal work function in *a* direction and *b* direction for the ML tellurene FETs. (b) Illustration of FLP in the ML tellurene transistor. *S* is the FLP factor.